J. Wind Eng. Ind. Aerodyn. 125 (2014) 168–179

Contents lists available at ScienceDirect

Journal of Wind Engineering and Industrial Aerodynamics

journal homepage: www.elsevier.com/locate/jweia

Unsteady flow simulation of a vertical axis augmented wind turbine: A two-dimensional study

Rosario Nobile [a,*], Maria Vahdati [b], Janet F. Barlow [c], Anthony Mewburn-Crook [d]

[a] Technologies for Sustainable Built Environment Centre, University of Reading, JJ Thompson Building, Reading RG6 6AF, United Kingdom
[b] School of Construction Management and Engineering, University of Reading, United Kingdom
[c] Department of Meteorology, University of Reading, United Kingdom
[d] Matilda's Planet Manufacturing Ltd., Margam Port Talbot, United Kingdom

ARTICLE INFO

Article history:
Received 13 March 2013
Received in revised form
2 December 2013
Accepted 3 December 2013
Available online 17 January 2014

Keywords:
Vertical axis wind turbine
Augmented wind turbine
Computational fluid dynamics
Turbulence model
Built environment

ABSTRACT

As the integration of vertical axis wind turbines in the built environment is a promising alternative to horizontal axis wind turbines, a 2D computational investigation of an augmented wind turbine is proposed and analysed. In the initial CFD analysis, three parameters are carefully investigated: mesh resolution; turbulence model; and time step size. It appears that the mesh resolution and the turbulence model affect result accuracy; while the time step size examined, for the unsteady nature of the flow, has small impact on the numerical results. In the CFD validation of the open rotor with secondary data, the numerical results are in good agreement in terms of shape. It is, however, observed a discrepancy factor of 2 between numerical and experimental data. Successively, the introduction of an omnidirectional stator around the wind turbine increases the power and torque coefficients by around 30–35% when compared to the open case; but attention needs to be given to the orientation of the stator blades for optimum performance. It is found that the power and torque coefficients of the augmented wind turbine are independent of the incident wind speed considered.

1. Introduction

Although the expansion and installation of wind turbines is mainly focused on rural and open areas, more recently the attention has also moved to the built environment. The benefits are mainly generation of electricity on the site where it is needed, and the reduction in transmission losses and cable costs (Mertens, 2006). The progress of small wind turbines in the built environment has been mainly concentrated on HAWTs, however, several studies have shown that VAWTs are more suitable for urban areas (Mertens, 2006; Mewburn-Crook, 1990; Stankovic et al., 2009; Ferreira et al., 2007a). The advantages are mainly: omnidirectionality without a yaw control; better aesthetics to integrate into buildings; more efficient in turbulent environments; and quieter in operation (Hofemann et al., 2008). Nevertheless, today a number of constraints such as low starting torque, high torque fluctuations and complex flow are holding back the potential market of VAWTs.

Recently, the wind energy sector has seen some researchers explore the concepts of augmented devices (Mewburn-Crook, 1990; Oman et al., 1976; Igra, 1977; Abe et al., 2005; Thomas, 1991). The concept has been around since the late 1960 s without having any industrial success, as most augmenters were unidirectional and added cost to the wind turbine (Mewburn-Crook, 1990). The theory behind augmented wind turbines (AWTs) has been revisited for the built environment in order to accommodate low wind speeds, and high turbulence that are typically found in these surroundings. Pope et al. (2010), in Canada, proposed and analysed an omnidirectional AWT; it is known as Zephyr vertical axis wind turbine, and it has been designed for the built environment. This AWT is composed of a stator–rotor configuration; the power coefficient C_p was proved to be around 0.12. Due to its low C_p values, however, this design was unacceptable for commercial applications. Tong et al. (2010), in order to overcome low wind speed in urban areas, have proposed an innovative power-augmentation-guide-vane (PAGV) design for a VAWT. The PAGV system is mainly designed to guide and increase the wind speed before entering the wind turbine. The geometry was optimised by running several CFD simulations; the numerical results predicted a power increment of 1.25 compared to an open VAWT of the same size. Takao et al. (2009) have proposed and tested a directed guide vane row to increase the performance of a straight-bladed VAWT. The focus was mainly on the geometry of the guide vane row for different combinations of setting angle and gap between rotor and guide vane row. The authors concluded that the peak coefficient is considerably higher than that of a wind turbine without guide

* Corresponding author. Tel.: +44 771 788 4099, +44 118 327 9577.
E-mail addresses: r.nobile@reading.ac.uk, rosario.nobile@gmail.com (R. Nobile).

0167-6105/$ - see front matter © 2014 Elsevier Ltd. All rights reserved.
http://dx.doi.org/10.1016/j.jweia.2013.12.005

vane. It was found that for a setting angle of 45° the power coefficient was 1.8 times higher than the open rotor; the gap between rotor and guide vane row did not have any effect on the power of the wind turbine. Similarly, Kirke (2011) has conducted a number of experiments to understand the performance of different hydrokinetic turbines with and without a diffuser. Since the data, for all tests with diffuser, did not consistently show an improvement of the power coefficient; it was concluded that the cost-effectiveness of the diffuser was doubtful.

In this paper a novel vertical axis augmented wind turbine (AWT), developed by Mewburn-Crook (1990) in collaboration with Balfour Beatty Ltd., is examined. The novel AWT, designed for the built environment, consists of a stator and rotor. The stator is composed of eight vertical blades, surmounted top and bottom by conical surfaces; the rotor is composed of three vertical blades that are attached to a central shaft with supporting arms.

In the initial CFD investigation, an open rotor was analysed in order to select the most appropriate mesh, turbulence model, and time step to be implemented for the consecutive numerical simulations. In this part, a CFD validation was performed with secondary data obtained from a similar rotor. Successively, the same rotor was combined with an augmented stator with the aim of increasing the power output of the wind turbine. Finally, a number of CFD simulations were examined with different orientations of the stator blades and different wind speeds, in order to understand how the performance of the augmented rotor is affected. The numerical results are compared and discussed in this paper.

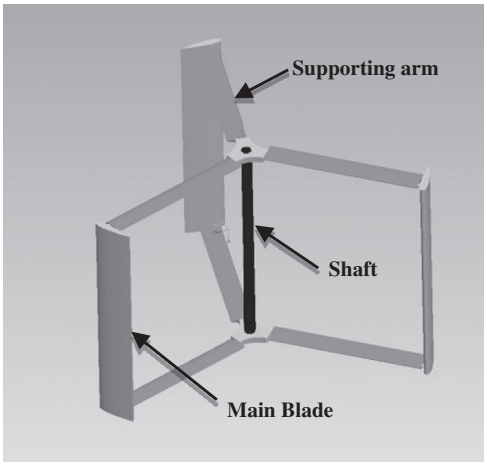

Fig. 1. The 3D open rotor of the AWT.

Table 1
Properties of the rotor.

NACA0018	Chord c (mm)	Thickness t (mm)	Span s (mm)	Quantity N (–)
Rotor blade	490	88.2	2,600	3
Supporting arm	250	45	1,800	6

2. The augmented wind turbine design and computational set-up

2.1. The components of the AWT

The 3D model was generated by using a solid CAD (ProEngineer Wildfire 4.0); the 2D models for both open and augmented rotor were extrapolated from the middle section of the 3D model. The 2D extrapolation was necessary in order to reduce computational time, and understand initially the aerodynamics involved during the operation of the wind turbine. In the present 2D numerical study, the effects from supporting arms and conical surfaces were not taken into consideration.

2.1.1. The rotor

Fig. 1 shows the rotor considered in the numerical study; it is a straight-bladed Darrieus (or Giromill) rotor with a diameter D_r of 4.2 m. The open rotor is composed of three blades, and each blade is attached to a central shaft by two supporting arms. The total number of supporting arms is 6, and the central shaft has a diameter D_{sh} of 0.06 m.

The aerofoil considered, for both vertical blades and supporting arms, is a symmetrical NACA 0018, and its characteristics are listed in Table 1. The rotor solidity σ_r is defined as N_C/R_r and is equal to 0.73. The pitch angle for both vertical and horizontal blades was set to zero degrees. The blade aspect ratio AR of the vertical blade is defined as s_r/c and is equal to 5.3. The pressure centre, in the midsection of the blade, is defined at 0.25c, with c representing the blade chord.

2.1.2. The stator

As shown in Fig. 2, the stator of the AWT is composed of eight straight vertical blades and two conical surfaces. The stator blades form eight identical and converging inlet surfaces to concentrate the mass flow rate next to the rotor; while the outer edges of the conical surfaces promote turbulent mixing above and below in order to reduce the back pressure inside the stator and increase the power output of the wind turbine. The aerofoil profile of the stator blades is also a NACA0018; the geometric properties for both vertical blades and conical surfaces of the stator are listed in Table 2. The internal diameter is 4.8 m, while the external diameter is 6.8 m.

The gap between stator and rotor (stator/rotor clearance) was set to 0.3 m with a stator/rotor turbine diameter ratio of 1.7.

2.2. The computational domain and meshing

As the aim of the present numerical investigation was to determine the operation of an open and an augmented three-bladed rotor of a Giromill wind turbine, the engagement of fixed and rotating domains were required. As shown in Fig. 3, the 2D fluid domain was composed of two distinct domains: a fixed rectangular outer domain with circular aperture; and a circular inner domain to fit into the aperture. The fixed rectangular outer domain was identified as the wind tunnel domain; the circular inner domain was identified as the rotor domain for the open wind turbine and stator–rotor domain for the AWT.

The individual geometries were modelled in ProEngineer Wildfire 4.0 and imported into ANSYS DesignModeler 14.0. The 2D open and augmented rotors were extrapolated from the middle plane of the original 3D model. The mesh was generated by employing the solver ANSYS CFX Meshing 14.0.

2.2.1. The wind tunnel domain

Fig. 4 shows the main dimensions and the boundary conditions employed in the wind tunnel domain. The wind tunnel domain represents the outside fluid around the open or the augmented rotor.

The width of the wind tunnel domain was set to 6 times the rotor diameter; a circular hole was placed in it to fit the rotor or

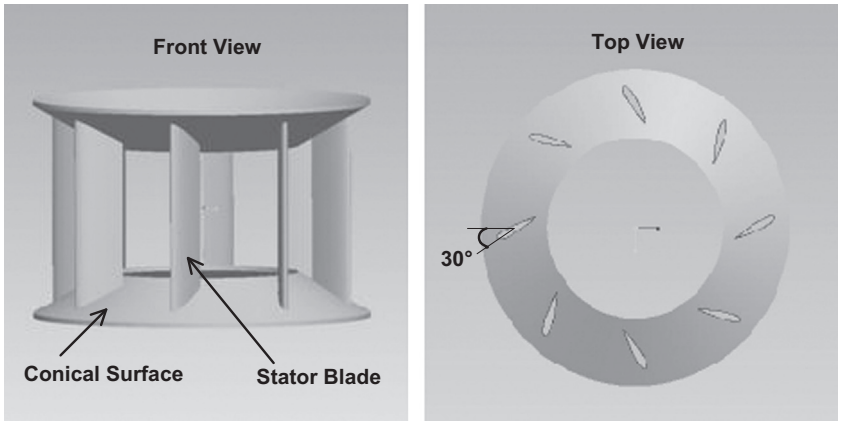

Fig. 2. Front and top views of the 3D stator of the AWT.

Table 2
Properties of the stator.

NACA0018	Chord c (mm)	Thickness t (mm)	Span In/Out s (mm)	Number N (–)
Stator Blade	1,000	180	2,600/3,600	8
Conical Surface	–	50	1,100	2

the stator–rotor domain. In accordance with Ferreira et al. (2007b): the inlet boundary condition was set to 10 rotor diameters upwind, as an inlet condition close to the rotor can give incorrect results; the outlet boundary condition was set to 14 rotor diameters downwind, in order to monitor wake formations during the operation of the wind turbine. The inlet boundary condition was defined at the left side of the wind tunnel, with a turbulence intensity of 10% in order to simulate the operation of the wind turbine in the built environment. The outlet boundary condition was defined at the right side of the wind tunnel with a relative pressure of 0 Pa; it represents an open condition. A structured mesh was employed for the fixed rectangular outer domain, with the intention of reducing computational time. Two wall boundary conditions, with free slip wall, were used for the side walls with the purpose of neglecting solid blockage effects. Two symmetry boundary conditions were considered for the top and bottom part of the wind tunnel domain, as the 2D model was extracted from the midsection of the 3D full model. An interface boundary condition was employed between the circular hole in the wind tunnel and the rotor (or stator–rotor) domain in order to guarantee fluid continuity and faster result convergence.

2.2.2. The rotor domain

Fig. 5 shows the boundary conditions and dimensions of the rotor subdomains inside and around the rotor. The rotor domain was split into two different subdomains: a circular subdomain around the rotor blades and a circular subdomain inside the rotor with a central shaft. For both subdomains, an angular velocity Ω was imposed.

The two subdomains were fitted into the circular hole of the wind tunnel domain, with the central shaft crossing the centre. The two subdomains were meshed by using unstructured elements, as they can follow complex geometries such as aerofoils. The two distinctive subdomains were created in order to have the freedom to change the mesh quality around the rotor and verify mesh dependency, which is explained in Section 2.4. Interface boundary conditions were used between the two subdomain sides in order to guarantee fluid continuity. For faster convergence, the size of the cells between the regions in contact was kept the same. Wall boundary conditions were imposed on the rotor blades and central shaft with zero velocity. Finally, symmetric boundary conditions were employed for the top and bottom part to represent that the 2D model was extrapolated from the midsection of the 3D model.

2.2.3. The stator domain

As shown in Fig. 6, the stator is characterised by 8 NACA0018 symmetric blades equally distributed around the rotor, with the location inside the circular hole of the wind tunnel.

An interface boundary condition was imposed between wind tunnel and stator domain. Wall boundary conditions were considered for all stator blades. Also symmetric boundary conditions were employed for the top and bottom part of the stator. The main reason for having a stationary ring around the stator blades is to control the mesh quality of this region. Similarly, for the stator domain an unstructured mesh was generated; as it is easy to implement and match with the rotor domain.

For a better understanding, Fig. 7 shows an example of the mesh used for the augmented rotor. As shown in Fig. 7, different sub–domains were created in order to achieve high quality mesh around and near both stator and rotor blades. It was necessary in order to detect boundary layer developments and wake generations from the blades of the AWT. In this paper, the wall y^+ was defined between 25 and 100, which is used in numerous CFD applications (Qin et al., 2011).

2.3. The flow solver and turbulence model

In order to understand the aerodynamics of the AWT, a CFD educational version of ANSYS CFX 14.0 was employed. The numerical solver used is based on solving the Reynolds Averaged Navier Stokes (RANS) equations by employing a finite-volume method.

A challenge in any CFD code is the selection of the right turbulence model, which is highly dependent on the nature of the flow considered. Its mathematical nature can affect computational resources, time and result accuracy. Wang et al. (2010) show that the most popular turbulence models, adopted in the CFD community, are mainly Direct Numerical Simulation (DNS), Large Eddy Simulation (LES) and Reynolds-Averaged Navier–Stokes (RANS). The DNS method requires a large amount of computing resources and time. The LES method is appropriate for 3D simulations. The method adopted for this 2D numerical study was the RANS method. The three RANS turbulence methods analysed, due

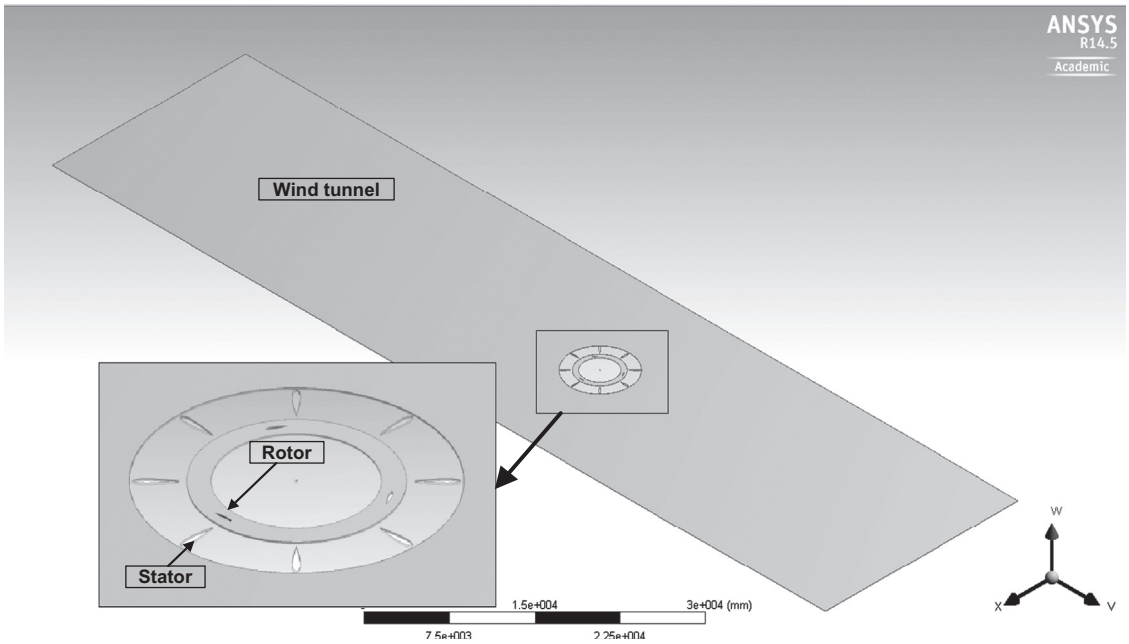

Fig. 3. The 2D fluid domain of the AWT studied during the CFD analysis.

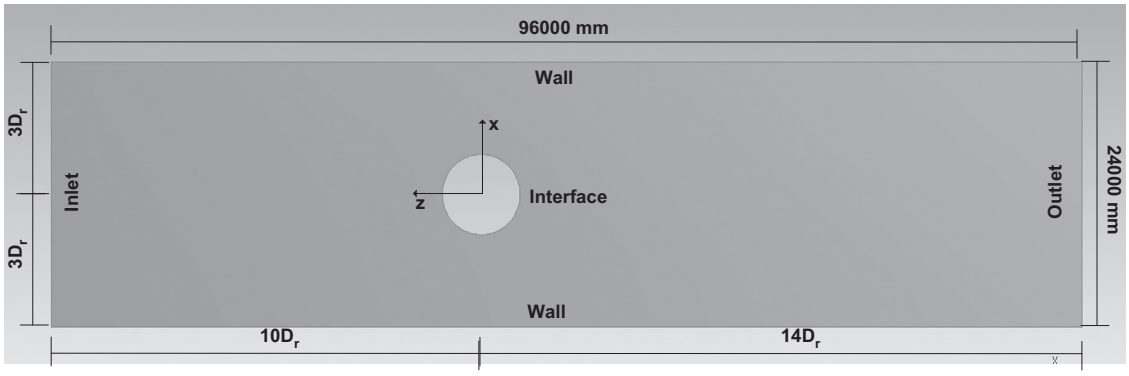

Fig. 4. Wind tunnel domain and boundary conditions (D_r=rotor diameter).

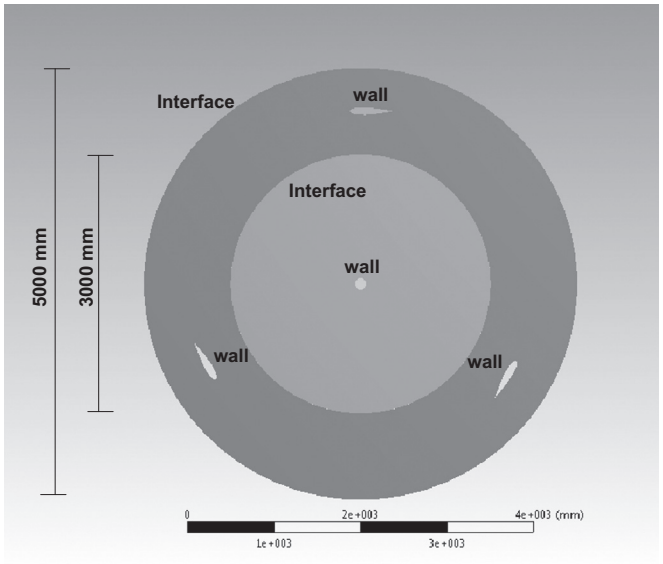

Fig. 5. Rotor domain and boundary conditions.

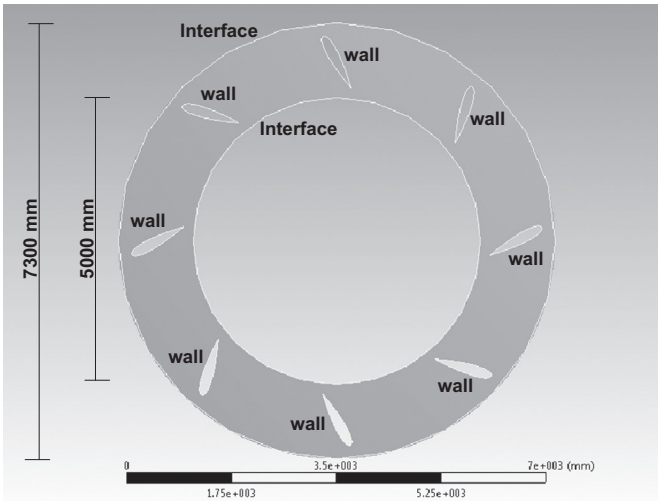

Fig. 6. Stator domain and boundary conditions.

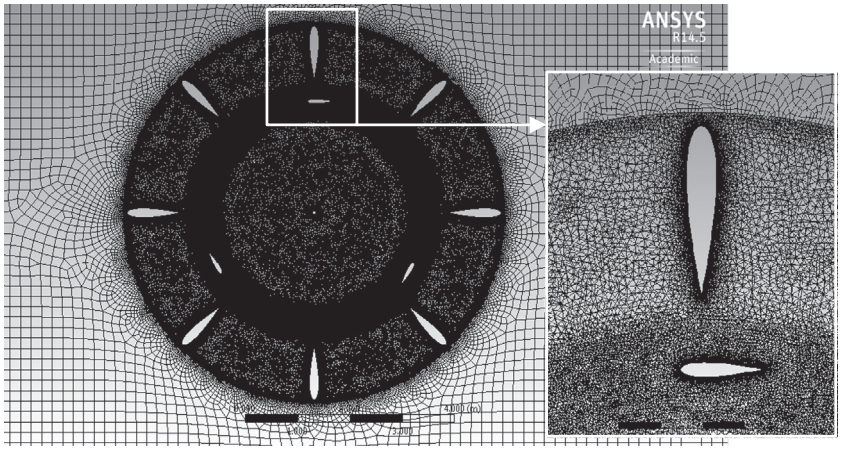

Fig. 7. Example of meshes used for different sub-domains of the augmented rotor.

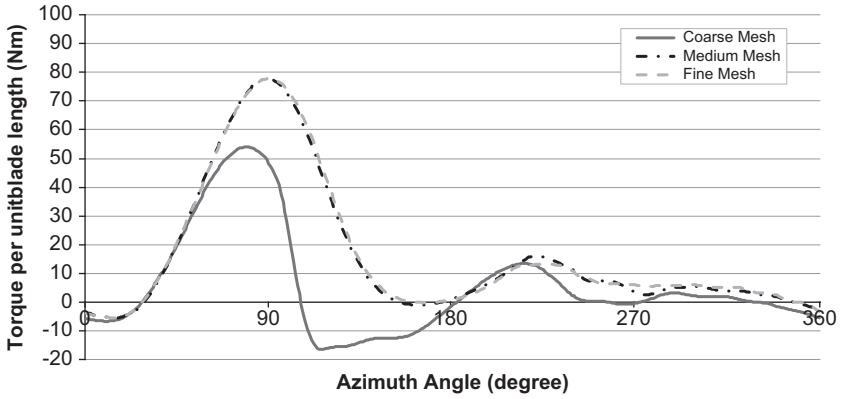

Fig. 8. Mesh dependency study for 2D open rotor.

to low computational costs and time, were: the standard k–ω model, the standard k–ε model and the Shear Stress Transport (*SST*) model. The three turbulence models considered are classified as two-equation turbulence models, as they include two extra transport equations to represent the turbulent properties of the flow. One variable determines the energy in the turbulence, while the other variable considers the scale of the turbulence.

2.4. Mesh dependency study

A number of simulations were carried out in order to determine how the mesh quality was affecting the CFD results. The objective was to select the most appropriate mesh that can guarantee low computational costs and good result accuracy. The case considered in this study was based on a three straight-bladed open rotor with wind speed $U_\infty = 6$ m/s and tip speed ratio $\lambda = 3$. This case was selected because the best performance of the wind turbine was expected to be achieved for a value around this TSR.

Fig. 8 shows the instantaneous torque per unit blade length versus azimuth angle; it refers to a single rotor blade and a complete rotation. The numerical study was run for three different mesh resolutions: coarse, medium and fine. As shown in Fig. 8, there is a good agreement between 0° and 30° among the three cases analysed; while there is a large difference in the solution for the coarse and medium meshes for azimuth angle between 30° and 180°, and small dissimilarity afterwards (180–360°).

Overall, as can be seen in Fig. 8, there is little difference in the solution between medium and fine meshes. It is also shown that for both medium and fine meshes the torque is positive with negative values only between 350° and 25°. Fig. 8 also shows that large amount of energy is generated in the upwind side, with the maximum value at 90°, while small amount of energy is extracted in the downwind side with a peak at about 220°.

Table 3
Number of elements and simulation time for the three meshes analysed.

Mesh resolution	Coarse mesh	Medium mesh	Fine mesh
Number of elements	21,000	360,000	2,000,000
Simulation time	1 h and 25 min	4 h and 34 min	17 h and 53 min

The number of elements and time for simulation, for the three cases analysed, are listed in Table 3. It is clear that the simulation time is highly dependent on the number of elements considered. It appears that the medium mesh is a good compromise in terms of computational costs. Consequently, the following mesh was employed for all the successive simulations considered in this study.

2.5. Time dependency study

A successive study was carried out in order to understand the sensitivity of the solution to time step selection. The unsteady nature of the flow, due to the rotation of the VAWT, was introduced by inserting a fourth variable into the numerical results, which was time. According to Qin et al. (2011), the time step used for each simulation needs to be selected with care in order to achieve good convergence in the final results.

Three different cases were examined, and distinguished as time step $dt = 0.003$, time step $dt = 0.002$ and time step $dt = 0.001$. The

results obtained for these different time step sizes are plotted in Fig. 9. It shows the instantaneous torque per unit blade length generated on a single rotor blade for a complete revolution of 360°. From Fig. 9, it appears that among the three different time step sizes there is little difference in the final results. Consequently, a time step of 0.003 s was selected for the successive numerical simulations in order to reduce computational time to a minimum.

2.6. Turbulence model study

In this numerical analysis, three different RANS turbulence models were considered: standard k–ε model, standard k–ω model and *SST* model. In this case a medium mesh and a time step of 0.003 s were selected in accordance to the previous sections.

Fig. 10 shows the instantaneous torque forces related to each turbulence model analysed. The respective values are referred to a complete rotation of a single rotor blade. It is clear from Fig. 10 that the standard k–ε model, in the upstream flow, results in lower torque generation than the standard k–ω and *SST* models. Both standard k–ω and *SST* models, however, show a good agreement in the upstream flow and small dissimilarities in the downstream flow.

It has been found that the *SST* model behaves well in adverse pressure gradients and separating flow, which are typically seen during the operation on any wind turbine. The principle behind the *SST* model is the combination of two different turbulence models: the k–ω model in the inner parts of the boundary layer, and the k–ε model in the free-stream. In addition, a previous study of Nobile et al. (2011) has shown that the *SST* model was able to simulate in more detail the vortices that are seen during dynamic stall at low TSRs than the k–ω and k–ε model. Therefore, the *SST* model was employed for all the successive numerical simulations analysed in this study.

Table 4
List of parameters presented in the equations above.

Parameter	Symbol	Unit
Incident wind speed	U_∞	[m/s]
Angular velocity	ω	[rad/s]
Rotor radius	R_r	[m]
Average power	P_{ave}	[kW]
Air density	ρ	[kg/m^3]
Average torque	T_{ave}	[Nm]
Rotor swept area	A_r	[m^2]

Table 5
Comparison between the two rotors.

Parameter	Open rotor (AWT)	Raciti Castelli et al. rotor
Blade profile	NACA0018	NACA0021
Rotor diameter [mm]	4,000	1,030
Simulation	2D	2D
Number of blade [–]	3	3
Chord [mm]	490	86
Solidity [–]	0.7	0.5

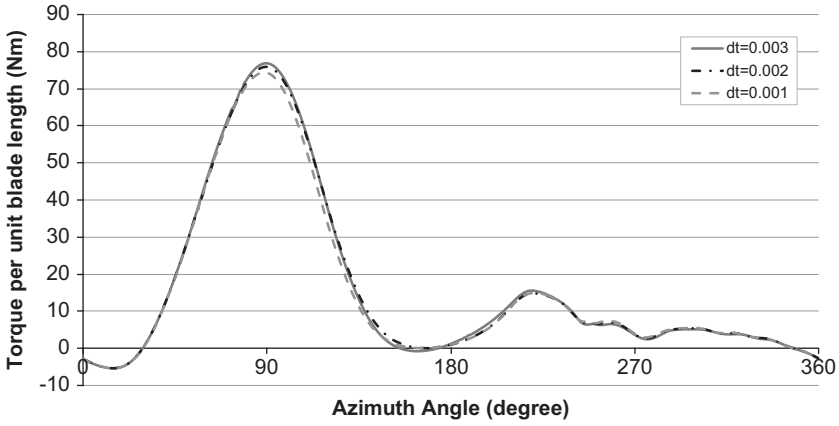

Fig. 9. Time dependency study for 2D open rotor.

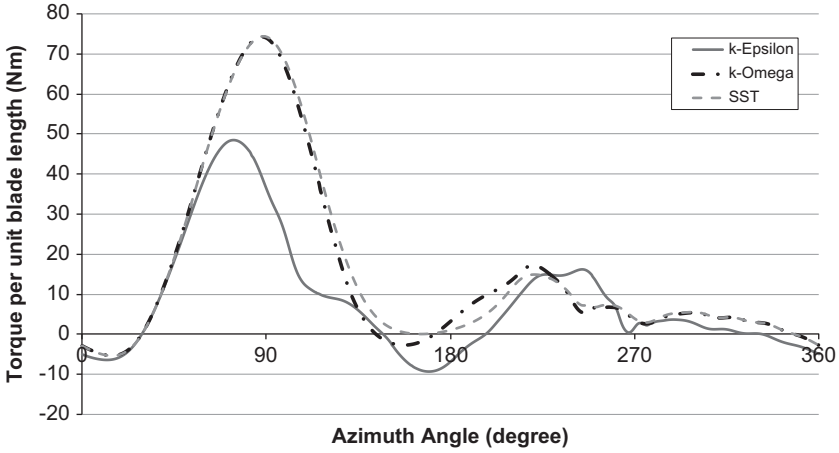

Fig. 10. Turbulence model study for 2D open rotor.

In this study, the respective variables monitored were the average torque and the power coefficients versus TSR. The average torque coefficient $C_{t,av}$ and the average power coefficient $C_{p,ave}$ are given by:

$$C_{t,ave} = \frac{T_{ave}}{0.5\rho A_r R_r U_\infty^2} \quad (1)$$

$$C_{p,ave} = \frac{P_{ave}}{0.5\rho A_r U_\infty^3} \quad (2)$$

and the tip speed ratio (TSR) as:

$$TSR = \frac{\omega R_r}{U_\infty} \quad (3)$$

In Table 4 are summarised all parameters listed above, with respective symbols and units.

2.7. CFD validation: open rotor

In this section, an empirical study was compared with the numerical simulations of the open rotor examined in this paper. The scope was to verify the accuracy of CFD data with experimental data. The relevant study was selected by considering a number of similarities with the open rotor. The main criteria for the selection were: straight three-bladed Darrieus rotor, symmetrical NACA series, and similar solidity. The most significant experimental data was obtained from a study by Raciti Castelli et al. (2011). In this study, the 2D rotor was analysed at 8 different rotational speeds with a constant wind speed of 9 m/s. As listed in Table 5, the chord and the diameter are 5.7 and 4 times smaller than the open rotor; the solidity, however, is of similar magnitude, 0.5 instead of 0.7.

Fig. 11 shows the numerical and experimental data obtained by Raciti Castelli et al. (2011). The numerical simulations were conducted with Fluent CFD, while the empirical analysis was performed in a low speed wind tunnel. Fig. 11 shows the average power coefficient $C_{p,ave}$ versus tip speed ratios (TSRs). It clearly seen that the trend of the two curves, numerical and empirical, is of similar shape with a constant discrepancy factor of 2. In Raciti Castelli et al. (2011), the maximum power coefficients, for both CFD and wind tunnel tests, are around a TSR of 2.50; the $C_{p,ave}$ is equal to 0.55 for the 2D and 0.3 for the wind tunnel. According to Raciti Castelli et al. (2011), the dissimilarity, between numerical and experimental data, could be associated with the effect of finite blade length and spoke drag that were not considered in the 2D numerical analysis. The authors, however, concluded that the CFD code was able to visualise the basic physics behind a VAWT, and it can be used as an alternative to wind tunnel tests.

Moreover, Fig. 11 also shows the $C_{p,ave}$ values of the 2D open rotor examined in this paper. Although there are geometrical differences between the two rotors (Table 5), the trend followed by the open rotor is of similar shape to the Raciti Castelli et al. (2011) study. It is clearly shown that for the open rotor the maximum value has moved around 10% up when compared to the rotor of Raciti Castelli et al. (2011). This is in agreement with the fact that the $C_{p,ave}$ increases as the solidity σ increases (Paraschivoiu, 2002), 0.7 as opposed to 0.5; but the $C_{p,ave}$ peak of the open rotor should be obtained for a lower TSR than the Raciti Castelli et al. (2011) case. The peak is at a TSR of 2.75, which is higher than 2.5 seen on Raciti Castelli et al. (2011). A possible explanation for this dissimilarity can be related to the difference in blade profiles.

As for the solidity σ, the Reynolds number Re is another important parameter that affects the performance of any wind turbine. In this case, the mean Reynolds number Re_m is evaluated for the two rotors. It is defined as:

$$Re_m = \frac{cU_\infty}{\nu} \quad (4)$$

where c is the chord length, U_∞ the incident wind speed and ν the kinematic viscosity of air at 1.0 Pa and 20 °C. Table 6 summarises the Reynolds parameters related to the two rotors; the Re_m of the open rotor (AWT) is about 4 times higher than the open rotor of Raciti Castelli et al. (2011) study. This also reinforces the fact that the peak $C_{p,ave}$ of the open rotor is higher than that of Raciti Castelli et al. (2011) case.

3. Results

In this section, the 2D results related to three different conditions of the AWT are presented. The respective numerical analyses were based on considering medium meshes and the *SST* turbulence method, in accordance with the previous Sections 2.4 and 2.6. The time step was set to 0.003 s and 10 interaction loops were defined for each time step, in order to achieve result convergence. The residual convergence criterion was set to 10^{-4} at each time step. The average number of elements for each case simulated was

Table 6
Reynolds number for the two rotors.

Case	c [m]	U_∞ [m/s]	ν [m^2/s]	Re_m [–]
Open rotor (AWT)	0.49	6	15.11×10^{-6}	1.9×10^5
Open rotor (Raciti et al.)	0.086	9	15.11×10^{-6}	5.1×10^4

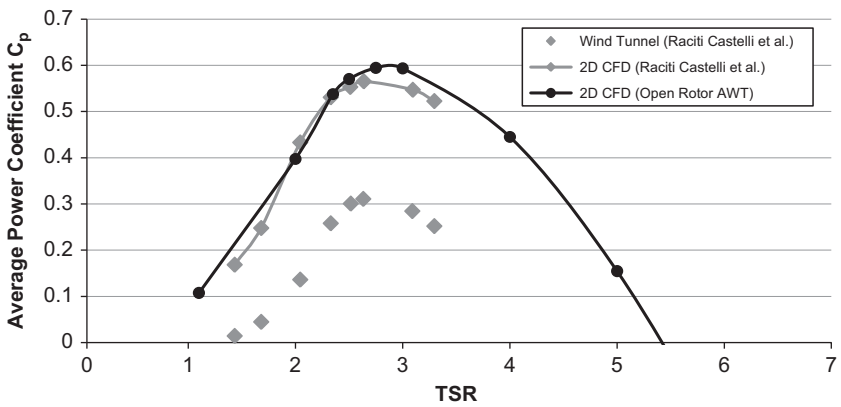

Fig. 11. Average power coefficient $C_{p,ave}$ versus TSR; a comparison between the two rotors.

around 1.0 million for the open rotor and 2.0 million for the augmented rotor. The whole number of revolutions was set to 5, in order to achieve periodical solution. The calculations were performed on a 4-core processor at 2.93 GHz clock speed.

In the first case, an open rotor was compared with an augmented rotor at incident wind speed U_∞ of 6 m/s over different TSRs. In the second case, the augmented rotor was examined over a range of TSR values for constant incident wind speeds (U_∞) of 6, 8, 10 and 12 m/s. In the third case the orientation of the stator blades was varied, while the rotor pitch angle was kept at 0°.

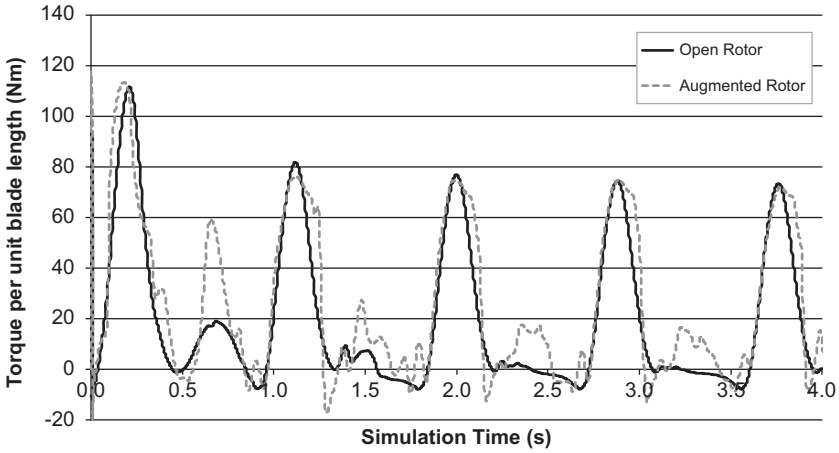

Fig. 12. Simulation convergence for 2D open and augmented rotor.

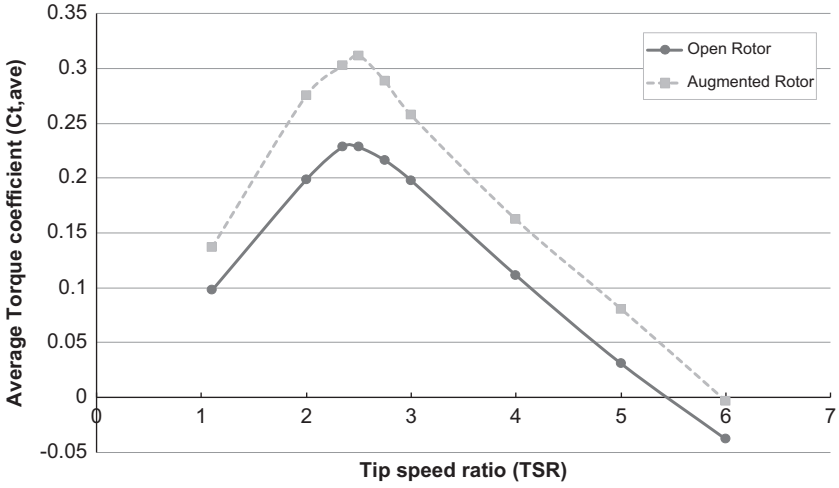

Fig. 13. Average Torque coefficient $C_{t,av}$ versus TSR for open and augmented rotor.

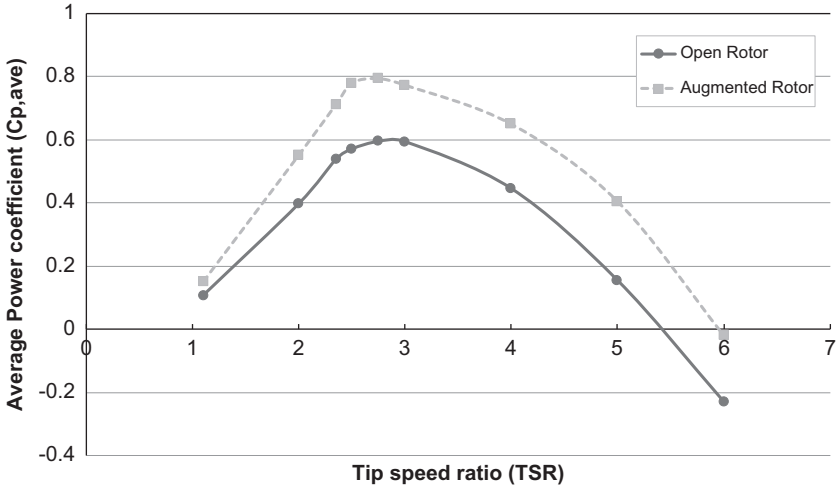

Fig. 14. Average Power coefficient $C_{p,ave}$ versus TSR for open and augmented rotor.

3.1. Case 1: open and augmented rotor

In Case 1, the power output of an augmented rotor was compared to an open rotor of the same dimensions and operating in similar conditions. The aim was to test if the introduction of an augmented device (stator) around the rotor blades is beneficial to the power output of the VAWT. An incident wind speed U_∞ of 6 m/s was chosen with the rotor operating at 9 different TSR values, for

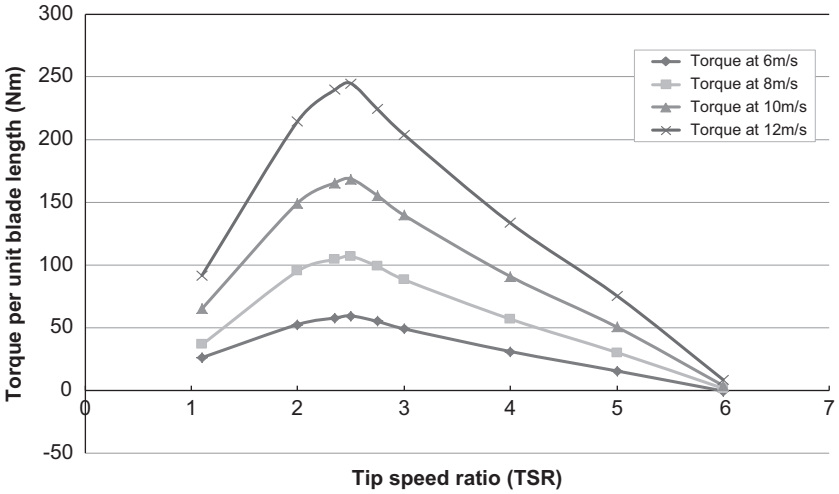

Fig. 15. Torque per unit blade length versus TSR for augmented rotor at different wind speeds.

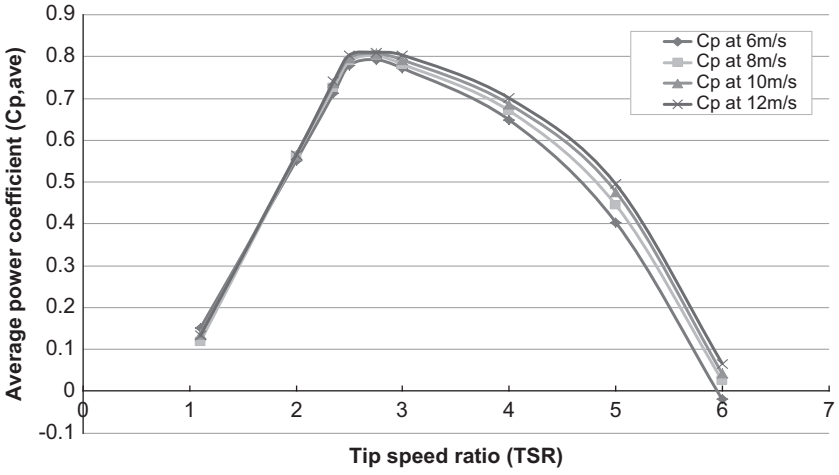

Fig. 16. Average Power coefficient $C_{p,ave}$ versus TSR for augmented rotor at different wind speeds.

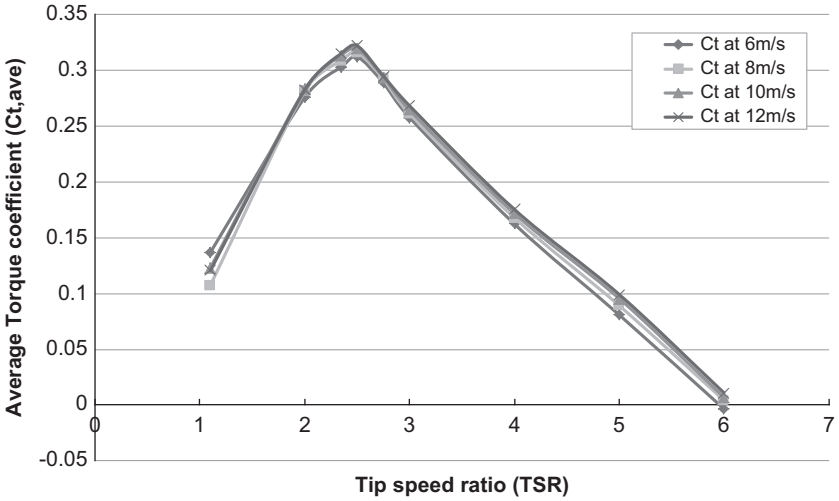

Fig. 17. Average Torque coefficient $C_{t,ave}$ versus TSR for augmented rotor at different wind speeds.

both open and augmented rotor. For the augmented rotor, the blades of the stator were fixed at 0°. The total number of CFD simulations analysed in this case were 18. For each simulation, the average computational time for the open rotor was around 8 h, while for the augmented rotor around 15 h. As shown in Fig. 12, each simulation run presented a degree of instability in the initial solution before achieving periodic values. It took some time for the lift to fully develop in the numerical simulation. Fig. 12 shows that, the CFD results were found to converge after 2 revolutions for the open rotor, and 3 revolutions for the augmented rotor.

Fig. 13 shows the $C_{t,av}$ versus 9 different TSRs for both open and augmented rotor. The dash line refers to the augmented rotor, while the solid line to the open rotor. As shown in Fig. 13, the augmented rotor has a higher $C_{t,av}$ than the open rotor. It is also shown a $C_{t,av}$ of the augmented rotor that has increased by 30% when compared to the case with the open rotor. As can be seen in Fig. 13, the highest $C_{t,av}$ for both augmented and open rotor is achieved at TSR of 2.50. The respective maximum $C_{t,av}$ values are 0.30 for the augmented rotor and 0.23 for the open rotor.

In a similar way, Fig. 14 shows the $C_{p,av}$ for both open and augmented rotor. For the open rotor (solid line), the maximum $C_{p,av}$ is closer to the Betz limit (0.593) with a TSR between 2.75 and 3.0. For the augmented rotor (dash line) the maximum theoretical $C_{p,av}$ is 1.34 times higher than the open rotor for a TSR of 2.75.

3.2. Case 2: augmented rotor at different wind speeds

In response to the fact that the power output of a wind turbine is highly dependent on the intensity of the wind, in Case 2 four different wind speeds were examined. The aim was to verify how the torque and the power generated were affected by different wind speeds and TSRs. Four constant wind speeds U_∞ were analysed: 6, 8, 10 and 12 m/s. For each wind speed U_∞, 9 different TSRs were considered in order to show the performance of the augmented rotor when operating both at optimum and lower values. The total number of simulations analysed are 36, with an average computational time of 2-day for each simulation. The variables monitored were average torque T_{ave} per unit blade length, average power coefficient $C_{p,ave}$ and average torque coefficient $C_{t,ave}$ versus TSR.

Fig. 15 shows the T_{ave} as a function of TSR for different wind speeds. As can be seen, the T_{ave} increases with the incident wind speed U_∞; it achieves the maximum value at TSR of 2.50, for each wind speed analysed. It is also shown that the T_{ave} peak at 12 m/s is four times higher than the peak at 6 m/s.

Fig. 16 shows the $C_{p,ave}$ of the augmented rotor as a function of TSR at four different incident wind speeds. The overall $C_{p,ave}$ follows the same trend independently of the wind speed considered. It is clearly shown that the maximum $C_{p,ave}$ value is achieved at TSR of 2.5. The maximum $C_{p,ave}$ is around 0.8 and it is 1.35 times higher than the open rotor. It can also be seen that for greater incident wind speeds the $C_{p,ave}$ increases slightly for TSR values higher than the maximum, while it is almost invariant on the left side.

Fig. 17 shows the $C_{t,av}$ as a function of TSR for four distinct wind speeds. It is clearly shown that the final values related to the $C_{t,av}$ at 9 different TSRs are also independent of the wind speed considered; the four curves are in good agreement. The maximum value 0.32 is achieved at TSR of around 2.5. It can also be seen that the $C_{t,av}$ increases with the TSR, with a peak value at TSR of 2.5, and then decreases linearly afterwards.

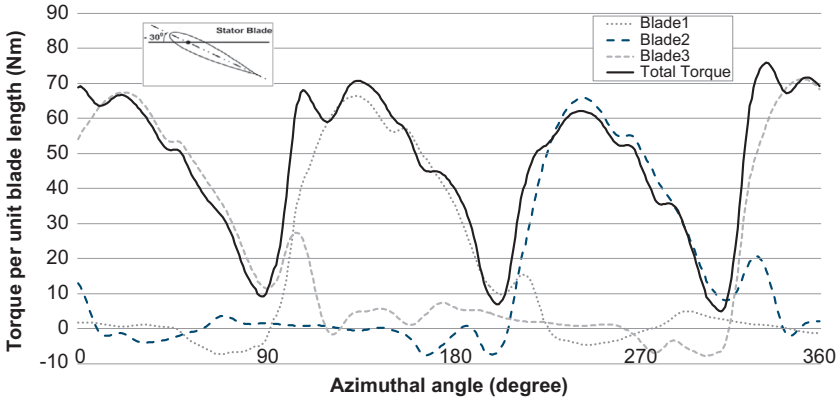

Fig. 18. Torque on AWT at −30° stator-blade orientation for a single revolution.

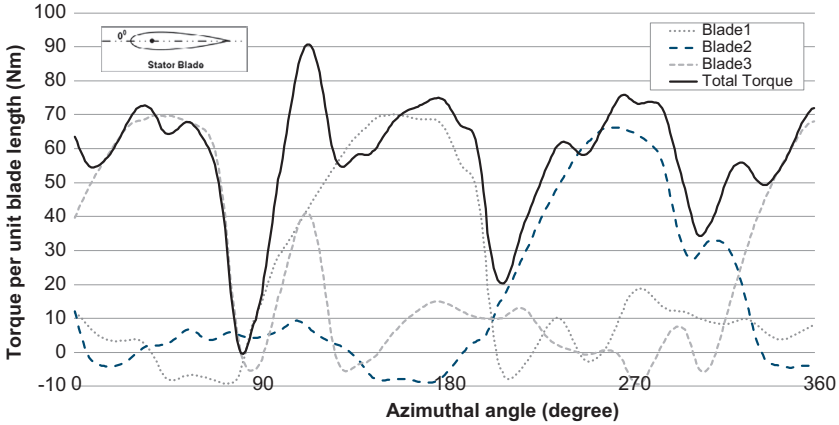

Fig. 19. Torque on AWT at 0° stator-blade orientation for a single revolution.

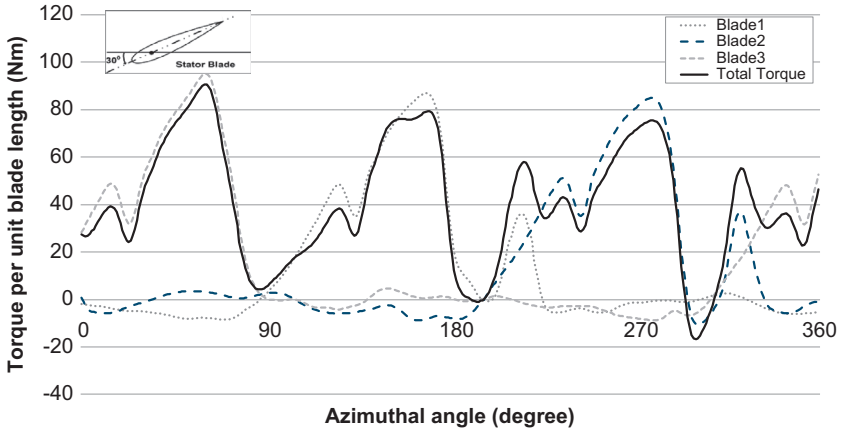

Fig. 20. Torque on AWT at 30° stator-blade orientation for a single revolution.

3.3. Case 3: augmented rotor at different stator blade orientations

Three different CFD simulations were considered, in order to understand how the rotor torque was affected by changing the orientations of the stator blades. For the rotor, the blade pitch was fixed to 0°, while for the stator the blade pitch was varied. The three different orientations analysed for the stator were −30°, 0° and 30°. The three CFD simulations were run at TSR of 2.50, as the previous study (Case 2) has shown maximum $C_{p,ave}$ at this TSR value. The incident wind speed U_∞ and the rotational speed Ω of the rotor were set to 6 m/s and 64 rpm. In this study, the monitored variables per revolution were instantaneous and total torque per unit rotor blade length. Figs. 18–20 below show the respective torque values at −30°, 0° and 30° stator-blade orientations. In each case, the torque values are referred to the 5th revolution, as it took 4 revolutions for the flow to become periodic.

Fig. 18 shows the instantaneous and total torque versus azimuthal angle per revolution, with the stator blades at −30°. As it can be seen, the instantaneous torque forces are referred to the three rotor blades, which are almost 120° apart from each other. The peaks for both instantaneous and total torque forces have moved to the right side when compared to the case with the open rotor in Section 2.4. For instance, the maximum torque on blade 1 is achieved around 130° instead of 90° of the open rotor. The torque area covered by the augmented rotor with the stator blades at −30° is greater than that with only the rotor. It also shows a number of torque peaks downstream, which are not shown in the open case. The average total torque (solid curve) is around 50 Nm per unit blade length and the area under each peak is almost equal with a period of 120°. It should be noted that in this case the total torque is always positive, with the torque value between 10 Nm and 70 Nm.

Fig. 19 shows the rotor torque values when the stator blades were orientated to 0°. In this case the average torque is greater than the previous case at −30°, with a value around 60 Nm. Fig. 19 shows that although the average torque per revolution is positive, there is a point where the torque is 0 Nm at around 90°. It also shows a fluctuating trend with a maximum value of 90 Nm at 110°. It should also be pointed out that the instantaneous torque forces move to the right side when compared to the open rotor, with more peaks and negative values than the previous case at −30°. Finally, Fig. 19 shows that high torque values are generated upstream; while downstream the values are higher when compared with the open rotor in Section 2.4.

Fig. 20 shows the instantaneous and total torque forces with the stator blades at 30°. In general, it can be seen that the total torque generated on the rotor blades is lower than the previous cases at −30° and 0°. The average torque value is around 40 Nm and is highly variable due to the presence of peaks and negative values. In Fig. 20, it can also be noticed that for some azimuthal positions the rotor is not self-starting due to negative values. As shown in Fig. 20, the instantaneous torque area for each rotor blades is significantly lower than the previous cases analysed. But overall, the instantaneous torque generated on each blade is similar in shape with small anomalies.

4. Discussion

A CFD tool can assist with the development of an AWT if the mesh resolution and the turbulence model are carefully selected. The time step size, however, has negligible impact on the CFD results. In the CFD validation of the open rotor, a good agreement has been found with secondary experimental data. Additionally, it appears that the introduction of an omnidirectional stator, around a VAWT rotor, can have a positive effect on the power generated, if it is properly designed.

As can be seen from Fig. 8 (Section 2.4), the mesh resolution plays a crucial role in the final CFD results, and particular attention needs to be given to it. The CFD elements or cells need to be sufficiently small to resolve boundary layers on the blade surfaces, and sufficiently big to avoid over-resolving regions of little interest. Fig. 8 also shows that for an open rotor the main energy extraction is achieved upstream with a maximum value at 90°, while there is a small amount of energy extracted downstream with a peak at 220°. The CFD results, related to a full rotation of an open rotor blade, are in good agreement with earlier CFD studies conducted by Qin et al. (2011) and Raciti Castelli et al. (2011).

In a similar way, the choice of a turbulence model can affect flow development, simulation time and result accuracy. In this CFD study only two-equation turbulence models were explored. Among the three turbulence models considered the k–ε model gave inaccurate results for the lift generated on the rotor blades; while the k–ω and *SST* turbulence models are in good agreement. From this study it appears that the k–ω model should be employed in studying the AWT because it is a good compromise in terms of results and computational time. However, the *SST* model was chosen for the successive analysis of the AWT, as a previous study (Nobile et al., 2011) showed that this model can accurately predict dynamic stall that is typically found in VAWTs at low TSRs.

The reason to study time step dependency was to detect in what way the simulation time could be reduced to a minimum without compromising result accuracy. The three different time steps analysed have shown small dissimilarities on final CFD results. Moreover, it has been shown that for each CFD simulation a number of revolutions are required to achieve periodic results. It

appears, in particular that for the open rotor the minimum number of revolutions was 2, while for the augmented rotor the number of revolutions required was 3. This difference can be explained by the fact that the introduction of an augmented device has increased the complexity of the flow around the same rotor and more revolutions are necessary for the lift to completely develop.

Three different cases were analysed for the augmented rotor. For Case 1, augmented rotor versus open rotor, it has been found that the use of an omnidirectional stator can increase the power output of the wind turbine. The introduction of converging surfaces upstream and diverging surfaces downstream has the advantage to accelerate and decelerate the flow in specific points of the rotor. Besides, the presence of shading regions generated by the stator blades upstream have also the potential to reduce drag forces seen on the rotor blades downstream. In contrast, for an augmented rotor, Fig. 12 (Section 3.1) shows that for both the upstream and downstream positions the rotor blades experience several peaks with an average torque value higher than the open case. The presence of an omnidirectional stator accelerates and directs the flow inside the rotor plane for a better energy extraction. In Case 2, augmented rotor versus incident wind speed, the dimensionless variables $C_{p,ave}$ and $C_{t,ave}$ were not affected by the incident wind speed considered. This can be explained by the fact that the order of magnitude of the Reynolds number from 6 m/s and 12 m/s is of similar range. Additionally, the torque generated at 12 m/s is 4 times the torque at 6 m/s, which is in good agreement with the theory (Eq. (1)). In Case 3, augmented rotor versus stator blade orientation, it has been shown that the orientation of the stator blades can substantially affect the power and performance of the AWT. In particular, it has been observed that at 0° and −30° orientations the torque has always positive values in contrast to 30° with some negative values.

5. Conclusion

In this paper the performance of an open and augmented rotor of a Darrieus straight-bladed VAWT has been presented. In the first part of the paper, an open rotor was examined in order to select a reasonable mesh resolution, turbulence model and time step to be implemented in the successive CFD simulations. A CFD validation of the open rotor was also conducted. In the second part of the paper, three different cases of the augmented rotor were examined in presenting power and torque coefficients and torque per unit blade length. In Case 1 the open rotor was compared to the augmented rotor under similar operational conditions. In Case 2 the performance of the same augmented rotor was tested under different incident wind speeds. In Case 3 the orientation of the stator blades was varied for a fixed rotor blade orientation and performance compared.

The paper has shown that the forces generated on the blades of an open rotor are highly dependent on the mesh resolution and turbulence model selected, while the time step used has small impact on the CFD results. The maximum energy extraction of the rotor is upstream with a maximum value at an azimuthal angle of 90°. The validation has shown that the CFD results were in good agreement with the empirical data examined. The main differences in values of the $C_{p,ave}$, can be associated with the fact that there were different Reynolds numbers and blade profiles. The introduction of an omnidirectional stator around the same rotor has the potential to increase the average power $C_{p,ave}$ and torque $C_{t,ave}$ coefficients by about 30–35% when compared to the open rotor with a TSR of 2.75. For the augmented rotor the orientation of the stator blades is fundamental for the performance of the AWT; it has been found that the best orientation is at 0° with an average torque of 60 Nm per unit blade length. It was found also that the power and torque coefficients of the augmented rotor are independent of the incident wind speed considered in this paper.

6. Future work

In this paper, only a specific direction of the incoming wind was examined when the stator was combined with the rotor. Future work could give consideration to the effect of wind direction on the aerodynamics of the stator. Further investigation of the comparison of CFD data of the augmented rotor with experimental data could be considered.

Future work could extend this study and assess 3D modelling of the AWT. This is fundamental for the future improvement of the AWT.

Acknowledgements

This work was completed under EPSRC Grant number EP/G037787/1 as part of the Technologies for Sustainable Built Environments (TSBE) Centre and a studentship provided by Matilda's Planet Manufacturing Ltd. (UK).

References

Abe, K., Nishida, M., Sakurai, A., Ohya, Y., Kihara, H., Wada, E., Sato, K., 2005. Experimental and numerical investigations of flow fields behind a small wind turbine with a flanged diffuser. J. Wind Eng. Ind. Aerodyn. 93, 951–970.

Ferreira, C.J., van Bussel, G., van Kuik, G., 2007a. 2D CFD simulation of dynamic stall on a vertical axis wind turbine: verification and validation with PIV measurements. In: Proceedings of the 45th AIAA Aerospace Sciences Meeting and Exhibit, American Institute of Aeronautics and Astronautics, pp. 1–11.

Ferreira, C.J.S., Bijl, H., Bussel, G. van, Kuik, G. van, 2007b. Simulating dynamic stall in a 2D VAWT: modeling strategy, verification and validation with particle image velocimetry data. J. Phys.: Conf. Ser. 75, 012023.

Hofemann, C., Simao Ferreira, C.J., Van Bussel, G.J.., Van Kuik, G.A.., Scarano, F., Dixon, K.R., 2008. 3D Stereo PIV Study of Tip Vortex Evolution on a VAWT. European Wind Energy Association EWEA, pp. 1–8.

Igra, O., 1977. The shrouded aerogenerator. Energy 2, 429–439.

Kirke, 2011. Tests on ducted and bare helical and straight blade Darrieus hydrokinetic turbines. Renew. Energy 36, 3013–3022.

Mertens, S., 2006. Wind energy in the built environment: concentrator effects of buildings (TU Delft).

Mewburn-Crook, A., 1990. The Design and development of an augmented vertical wind turbine.

Nobile, R., Vahdati, M., Barlow, J.F., Mewburn-Crook, A., 2011. Dynamic stall for a Vertical Axis Wind Turbine in a Two-dimensional Study. Linköping, Sweden.

Oman, R.A., Foreman, K.M., Gilbert, B.L., 1976. Investigation of diffuser-augmented wind turbines.

Paraschivoiu, I., 2002. Wind Turbine Design: With Emphasis on Darrieus Concept. Polytechnic International Press, Canada.

Pope, K., Rodrigues, V., Doyle, R., Tsopelas, A., Gravelsins, R., Naterer, G.F., Tsang, E., 2010. Effects of stator vanes on power coefficients of a zephyr vertical axis wind turbine. Renew. Energy 35, 1043–1051.

Qin, N., Howell, R., Durrani, N., Hamada, K., Smith, T., 2011. Unsteady flow simulation and dynamic stall behaviour of vertical axis wind turbine blades. Wind Eng. 35, 511–528.

Raciti Castelli, M., Englaro, A., Benini, E., 2011. The Darrieus wind turbine: proposal for a new performance prediction model based on CFD. Energy 36, 4919–4934.

Stankovic, S., Campbell, N., Harries, A., 2009. Urban Wind Energy.

Takao, M., Kuma, H., Maeda, T., Kamada, Y., Oki, M., Minoda, A., 2009. A straight-bladed vertical axis wind turbine with a directed guide vane row—effect of guide vane geometry on the performance. J. Therm. Sci. 18, 54–57.

Thomas, R.N. Vertical windmill with omnidirectional diffusion, (1991), (Google Patents).

Tong, C.W., Zainon, M.Z., Chew, P.S., Kui, S.C., Keong, W.S., Chen, P.K., 2010. Innovative power-augmentation-guide-vane design of wind-solar hybrid renewable energy harvester for urban high rise application. AIP Conf. Proc. 1225, 507–521.

Wang, S., Ingham, D.B., Ma, L., Pourkashanian, M., Tao, Z., 2010. Numerical investigations on dynamic stall of low Reynolds number flow around oscillating airfoils. Comput. Fluids 39, 1529–1541.